ORIGINAL PAPER

Large-scale simulations of wormhole growth in dissolving porous media using lattice Boltzmann method

Michał Dzikowski[1,2] · **Piotr Szymczak**[1]

Received: 17 April 2025 / Accepted: 16 February 2026

Abstract

We present a high-performance numerical algorithm for simulating the dissolution of porous media based on the Darcy-Brinkman model. The code utilizes recent developments in the lattice Boltzmann method to achieve high stability and performance gains. To the best of our knowledge, this is the first use of the lattice Boltzmann method as a fixed-point solver for problems with significant time-scale separation. The simulations enable the study of the development of reactive-infiltration instabilities in heterogeneous media, particularly in natural rocks, at high spatial resolutions. They reveal the formation and growth of highly conductive dissolution channels (wormholes), as well as the competition between them for flow and reactant flux. The transition from Darcy to Stokes flow is observed within the dissolution channels. We argue that there exists a minimum resolution at which the simulations need to be run in order to obtain a faithful representation of the geometry of the dissolution channels. At lower resolutions, the channels become straight, bulkier, and less ramified. We show that this minimum resolution is associated with the correlation length of the porosity field, establishing a critical link for accurate simulation fidelity. The results demonstrate the potential of next-generation supercomputers, based on GPGPU-based parallel computation, for predictive simulation of dissolution processes in porous media at experimentally relevant length scales and high resolutions.

Keywords Lattice-Boltzmann method · Dissolution · Reactive flow · Reactive-infiltration instability · HPC · CUDA · HIPP

1 Introduction

Chemical reactions between solutes and solids may gradually alter the composition and structure of the solid matrix, either creating or destroying permeable paths for fluid flow. Complex, dynamic feedback thus arises where, on one hand, fluid flow affects the characteristics of the solid medium, and on the other hand, the changing medium influences the fluid flow. Such feedback between the flow of fluids and the media through which they flow is essential for understanding the slow processes that, over geological timescales, may transform rock masses

Nonlinear couplings between flow and dissolution may lead to the appearance of instabilities resulting in the formation of various geological patterns. Particularly relevant for the present study is the so-called reactive-infiltration instability [1]: a relatively small change in pore geometry due to dissolution can result in a variation of permeability, focusing the flow and leading to further erosion. As a result, small inhomogeneities tend to grow and transform into highly permeable, finger-like flow channels, known by different names depending on the field. In the petroleum industry, they are referred to as "wormholes" [2] due to their similarity to tunnels dug by worms,

https://doi.org/10.1007/s10596-026-10410-z

whereas geologists call them "solution pipes" [3–5]. Such phenomena can be observed over a wide range of time and length scales: karst development takes thousands of years, whereas industrial acidization is performed over hours or days.

Spontaneous channeling of a dissolution front is crucial in many geophysical processes, such as diagenesis [6, 7], melt migration [8, 9], Terra Rosa formation [10], the development of limestone caves [11–13], and sinkhole formation [14]. Wormholes also play an essential role in various applications: CO_2 sequestration [15], risk assessment of contaminant migration in groundwater [16], and stimulation of petroleum reservoirs [2, 17–19]. Selecting the optimal flow rate is a critical issue in reservoir stimulation to achieve the maximum increase in permeability for a given amount of reactant [20–24], which is obtained in the wormholing regime. On the other hand, wormhole formation can undermine dam stability by promoting the breakthrough of highly permeable channels through its base [25]. Notwithstanding their practical importance, wormholes are, above all, beautiful examples of a pattern-forming system driven by a strong, nonlinear coupling between flow, reactive transport, and geometry evolution. Similar processes are involved in the formation of other branched structures, including leaf venation, river networks, and even vascular systems [26].

Recent years have witnessed a growing number of experimental studies on dissolution-induced morphology evolution [27–30], with many conducted in the context of CO_2 sequestration [31–37]. Given that many potential reservoirs for CO_2 storage are in carbonate strata, it is crucial to understand how the flow of CO_2-acidified brine impacts the long-term changes in porosity and permeability of the reservoirs and how it affects the caprock properties.

Most of the systems analyzed in these studies are relatively small (0.1 - 10 cm in length); however, even at that scale, a strongly non-uniform character of dissolution manifests itself profoundly, leading to the formation of wormholing patterns. Due to the self-similar nature of the flow-focusing process [38, 39], one can expect to find dissolution channels at all scales, up to the system size. This is indeed the case, with karst solution pipes appearing in many places worldwide [3–5, 40], most of them on a 1-10m scale, although much longer structures, up to kilometer-scale lengths, have also been reported [41].

Alongside the experimental studies and field observations, numerical models to study dissolution-induced flow focusing have also been developed. These models fall into three major categories:

1. Pore-scale numerical simulations, which were first introduced in [42], but they have become more widely used only recently [43–50] due to the rapid increase in computational power. Although these models are computationally intensive, they provide detailed information on spatial distributions of physicochemical variables and the temporal evolution of pore space micro-architecture without invoking effective parameters such as mass transfer coefficients. However, their computational cost limits their application mainly to micro-scale systems.
2. Darcy-scale or continuum-scale models, such as CrunchFlow [51], Min3P [52], PFLOTRAN [53], and Toughreact [54], which are based on continuum equations with effective variables like dispersion coefficients, Darcy velocity, and bulk reactant concentrations. These averaged variables replace the microscopic diffusion constant, fluid velocity, and reactant concentration. The application of Darcy-scale models is limited due to uncertainties associated with local constitutive equations and the upscaling limitations [55, 56], particularly at high reaction rates [57].
3. Network models, which introduce a simplified representation of porous material, either as a network of interconnected capillaries [2, 39] or as spherical pore bodies connected by cylindrical throats [58, 59]. To simulate the increase in permeability, the diameter of each network segment is increased in proportion to local reactant consumption. These models offer the advantage of allowing control over the pore architecture (diameters, lengths, connectivity), enabling tuning to represent different rocks. However, due to simplifying assumptions (cylindrical/spherical pores, mixing at the intersections, etc.), achieving a one-to-one representation of a given experiment in the network model is difficult.

The motivation for this work was to develop predictive numerical models for dissolution experiments on rock cores, leveraging high-resolution initial geometric data obtained from X-ray CT scans. The typical size of these cores (approximately 10 cm) precludes the use of a pore-scale approach, directing our focus toward Darcy-scale models. However, wormholing is a particularly demanding test case for such continuum descriptions, because the process is extremely sensitive to small-scale heterogeneities. Experiments and simulations have shown that both the onset of individual wormholes and their subsequent competition and branching are strongly influenced by subtle variations in porosity, permeability, mineralogy, and fracture structure [11, 60–64]. Pre-existing heterogeneity in the porosity field is not required for the reactive–infiltration instability to occur: a uniform medium with a planar front is already linearly unstable [1]. However, heterogeneity plays an important selection role: it determines where the first channels nucleate and how they compete and merge, and it influences the geometrical characteristics of the resulting dissolution patterns, with more tortuous and branched wormholes prevailing in heterogeneous systems. As the wormhole advances through the core, it is guided by local regions of higher permeability, such as microvugs that attract its tip, and deflected by denser regions such as microcementations and laminations [65, 66].

These considerations have important implications for modelling. Effective Darcy-scale models with relatively large mesh sizes tend to smooth out these inhomogeneities, resulting in wormholes that are considerably less tortuous than their natural counterparts. To obtain realistic numerical predictions, a high spatial resolution is therefore required, which in turn leads to substantial computational costs. To address this challenge, we adopted the lattice Boltzmann method due to its scalability and parallel-processing capabilities, which make it suitable for high-resolution simulations on modern GPU-based supercomputers.

2 Numerical model

In this work, we will focus on a Darcy-scale description of the flow in porous media, in which the internal properties of the porous material are described using averaged quantities. Fluid flow is described by the Darcy-Brinkman equation [67]:

$$\begin{cases} \nabla \cdot \mathbf{u} = 0, \\ \rho \frac{\partial \mathbf{u}}{\partial t} = \nabla p - \mu_{\text{eff}} \Delta \mathbf{u} - \mu \kappa^{-1} \mathbf{u}. \end{cases} \tag{1}$$

Here, $\mathbf{u}$ and p represent the average fluid velocity and pressure. Additionally, κ represents permeability, μ represents the molecular viscosity of the fluid, and μ_{eff} represents the effective viscosity of the medium.

It is important to stress that, although we use a lattice Boltzmann solver, our simulations are not pore-scale (grain-resolved) Navier–Stokes computations, but mesoscopic Darcy–Brinkman simulations. Each lattice cell represents a small mesoscopic averaging volume in which porosity φ and permeability $\kappa(\varphi)$ are defined. The grid spacing is comparable to, or a few times larger than, typical pore/throat sizes, but still many orders of magnitude smaller than the core length scale. Thus a single cell is smaller than a strict Darcy REV, and the model should be viewed as a Darcy–Brinkman description with locally averaged properties, rather than a full pore-scale DNS.

The transport of reactive species is described by

$$\frac{\partial \varphi c}{\partial t} + \nabla \cdot (\mathbf{u} c) = \nabla \cdot \mathbf{D} \nabla c - R, \tag{2}$$

where φ is the porosity, c is the average concentration of the reactive species, R is the reaction rate and D is the dispersion tensor.

Finally, the chemical erosion equation, which describes the increase in local porosity resulting from dissolution, is given by:

$$c_{\text{sol}} \frac{d\varphi}{dt} = \nu R(c, \varphi). \tag{3}$$

Here, $c_{\mathrm{sol}} = 1/v_m$ represents the molar concentration of the mineral phase, with v_m denoting the molar volume of the dissolving mineral, and ν is a stoichiometric coefficient. For instance, in the dissolution of limestone by acidic fluid:

$$\mathrm{H}^+ + \mathrm{CaCO}_3 \rightarrow \mathrm{Ca}^{2+} + \mathrm{HCO}_3^-.$$

Here, v_m corresponds to the molar volume of calcium carbonate, and ν is equal to 1, as one H^+ ion is required to dissolve a single CaCO_3 molecule.

To proceed, we introduce several simplifying assumptions. In particular, following Brinkman [67], we assume that the effective viscosity is identical to the molecular viscosity, $\mu_{\mathrm{eff}} = \mu$. More sophisticated models exist in which μ_{eff} depends on porosity [68–70], but there is no general consensus on the dependence of $\mu_{\mathrm{eff}}(\mu, \varphi)$ in the general case.

Next, we assume that the dispersion tensor is constant and isotropic, $\mathbf{D} = D\mathbf{I}$. This is an approximation sometimes adopted in theoretical considerations [71], as it allows for an analytical derivation of the instability wavelength in dissolving porous media. In general, $\mathbf{D}$ will be a function of both φ and $\mathbf{u}$ [21, 70]. In principle, this can be incorporated into the numerical framework. However, it should be noted that the lattice Boltzmann method (LBM) becomes unstable as $D \rightarrow 0$. Such cases become particularly challenging if $D \rightarrow 0$ only in some subset of the domain. Adequate treatment of these cases requires LBM collision operators for nonlinear advection-diffusion equations (ADE). For details, see [72, 73] and the references therein.

In this work, we assume a single-species, linear dissolution kinetics described by the equation:

$$R(c) = r_0 s(\varphi) c. \tag{4}$$

Here, r_0 represents the reaction rate constant, and s is the specific reactive surface area. This model can be generalized to include multiple reactive species and nonlinear reaction rates. However, the linear model is directly applicable to a wide range of different systems, including the acidization of limestone cores [2], karst formation [74], dissolution of gypsum [75], halite [14], and numerous other minerals.

To fully close the system, we need constitutive relations for $\kappa(\varphi)$ and $s(\varphi)$. For permeability, we use the Carman-Kozeny equation [76]:

$$\kappa(\varphi) = \kappa_0 \frac{\varphi^3}{(1-\varphi)^2}. \tag{5}$$

As for the specific reactive surface area we will either assume that it does not change as a result of the dissolution, $s(\varphi) = s_0 = \text{const.}$, or we will adopt a simplified version of the sugar lump model [77]:

$$s(\varphi) = 4 s_0 \varphi (1-\varphi), \tag{6}$$

which vanishes both as φ approaches 1 (indicating no more soluble substance to dissolve) and as φ approaches 0 (indicating no contact between water and rock).

Dissolution occurs on a characteristic time scale $t_d = (\nu\, r_0\, s(\varphi_0)\, \gamma)^{-1}$, where the acid capacity number, $\gamma = c_0/c_{sol}$, represents the ratio of aqueous ion to mineral concentrations, with c_0 denoting the reactant concentration at the inlet of the system. Typically, $\gamma \ll 1$, hence the time scales for dissolution are much larger than either concentration or velocity relaxation times [78]. This means that the time derivatives in flow and transport equations can be neglected, which is a significant theoretical and computational simplification.

The equations above are supplemented by boundary conditions for the velocity and concentration fields. At the inlet of the system we place a reservoir with $\varphi = 1$ and a length of 0.1 of the domain length (L_x). A constant velocity $u_0\mathbf{e}_x$ and concentration c_0 is imposed at the inlet of the buffer zone.

$$\begin{cases} u|_{\text{buffer inlet}} = u_0\mathbf{e}_x, \\ c|_{\text{buffer inlet}} = c_0. \end{cases}$$

This buffer acts as a flow distributor in a manner similar to experimental studies and is not represented in figures.

At the outlet of the domain, we have the following conditions:

$$\begin{cases} p|_{\text{outlet}} = 0, \\ \mathbf{n} \cdot \nabla c|_{\text{outlet}} = 0. \end{cases}$$

The system is assumed to be periodic in direction perpendicular to the flow (along y).

The relative importance of convective, diffusive and reaction processes in the system are measured by the Péclet number and Damköhler number. The former is defined as [79]

$$\mathrm{Pe} = \frac{u_0}{Ds(\varphi_0)\varphi_0}, \tag{7}$$

and measures the relative magnitude of convective and diffusive fluxes. On the other hand, the Damköhler number

$$\mathrm{Da} = \frac{r_0 s(\varphi_0) L}{u_0} \tag{8}$$

relates the surface reaction rate to the fluid flux.

The channelization observed in our simulations is the well-known reactive–infiltration instability. A planar dissolution front in a medium where permeability increases with porosity ($\mathrm{d}\kappa/\mathrm{d}\varphi > 0$) is linearly unstable over a broad range of parameters: for Damköhler numbers $\mathrm{Da} = \mathcal{O}(1)$ and Péclet numbers $\mathrm{Pe} \gtrsim 1$, advection and reaction reinforce small porosity and permeability perturbations faster than diffusion can smooth them out, so that such perturbations grow into fingers and wormholes [1, 71, 80, 81]. This instability is a property of the continuum model itself, and in our simulations it is triggered by small perturbations (numerical noise or imposed heterogeneity) and subsequently amplified by the nonlinear porosity–permeability feedback.

We use the lattice Boltzmann method (LBM) as the numerical solver for both the Darcy–Brinkman flow and the transport equation. Although LBM is intrinsically time dependent, it can also serve as a robust tool for quasi-steady problems. In our implementation, LBM is employed within a fixed-point iteration: for each physical time step of the dissolution problem, several LBM pseudo-time steps are performed to relax the velocity and concentration fields towards the quasi-steady solution consistent with the current porosity field. In this way, LBM acts as a fixed-point solver for a problem with strong separation between flow/transport and dissolution time scales. We developed a large-scale LBM-based solver for dissolution processes in porous media on top of the open-source, highly parallel multi-GPU TCLB code [82]. The main advantage of this approach is its high number-crunching performance, resulting from the strongly GPU-optimised design.

2.1 Structure of the algorithm

The time evolution of the system is governed by Eq. 3, which is discretized using the second-order trapezoidal rule, resulting in the following equation:

$$\varphi_{n+1} = \varphi_n + \frac{\Delta t\, \nu}{2c_{sol}} \left(R(\varphi_n, c(\varphi_n)) + R(\varphi_{n+1}, c(\varphi_{n+1})) \right). \tag{9}$$

The concentration field c depends on porosity both directly (via reactive surface area) and indirectly through the velocity field, which is also porosity-dependent. Resolving the time-marching Eq. 9 involves solving a nonlinear problem. To address this, we use fixed-point iterations of the form:

$$\varphi_{n+1}^{k+1} = \varphi_n + \frac{\Delta t\, \nu}{2c_{sol}} \left(R(\varphi_n, c(\varphi_n)) + R(\varphi_{n+1}^k, c(\varphi_{n+1}^k)) \right). \tag{10}$$

Here, k indexes the successive iterations. For each iteration, we solve for the flow and concentration fields using the Lattice Boltzmann Method, with k representing a single pseudo-time-step inside the solver. As a result, local porosity is updated in every LBM step. The steady state reached by the LBM solver represents the convergence of fixed-point iterations. It is essential to note that the intermediate solutions obtained during the LBM loop do not represent the physical time evolution of φ but rather intermediate solutions of a nonlinear problem.

To ensure proper mass conservation in the system, we take care when evaluating $R(\varphi_{n+1}, c(\varphi_{n+1}))$ to prevent porosity overshooting, where $\varphi_{n+1} > 1$. Formally, $s(\varphi)$ is defined only over the interval $0 \leq \varphi \leq 1$, but it can be extended outside of this domain by setting $s(\varphi) = 0$. This makes the right-hand side of Eq. 9 piecewise smooth, which means that the second-order approximation spanning the interval t_n, t_{n+1} will generally lead to an improper solution for $\varphi(t^*) = 1$, if $t^* \in (t_n, t_{n+1})$. To address this issue, we locally reduce the order of approximation to ensure global mass balance. This is done when the overshoot condition is met:

$$\varphi_n + \frac{\Delta t\, \nu}{2c_{sol}} \left(R(\varphi_n, c(\varphi_n)) + R(\varphi_{n+1}^k, c(\varphi_{n+1}^k)) \right) > 1. \tag{11}$$

When this condition is detected, we use implicit Euler approximation:

$$\varphi_{n+1}^{k+1} = \varphi_n + \alpha \frac{\Delta t\, \nu}{c_{sol}} \left(R(\varphi_{n+1}^k, c(\varphi_{n+1}^k)) \right). \tag{12}$$

Here, $\alpha \in (0, 1)$ and $t^* = t_n + \alpha \Delta t$. This method ensures that $\varphi_{n+1}^{k+1} = 1$ at the end of the time step.

For a fully consistent solution, it would be best to choose α globally as the minimum value over all relevant nodes. However, this would significantly reduce the time-step size, slowing down the code's execution. In this work, we consider α as a local scaling factor for reactivity R_0, leading to the following equation:

$$R(\varphi_{n+1}^k, c(\varphi_{n+1}^k)) = c_{sol} \frac{1 - \varphi_n^k}{\Delta t \nu}. \tag{13}$$

This limits the effective reaction rate during the last time step of dissolution at a given point in such a way that $\varphi = 1$ at the end of the time step.

2.2 Lattice Boltzmann reactive transport solver

The Lattice Boltzmann Method (LBM) in this work is used to obtain the steady-state solution of the following system of equations:

$$\begin{cases} \nabla \cdot \mathbf{u} = 0, \\ \nabla p - \mu_{eff} \Delta \mathbf{u} - \frac{\mu}{\kappa} \mathbf{u} = 0, \\ \nabla \cdot (\mathbf{u} c) = \nabla \cdot D \nabla c - R. \end{cases} \tag{14}$$

LBM time-marching is employed to update φ within fixed-point iterations. The utilization of an LBM solver in this manner has been present in the literature since the advent of the method, and numerous numerical techniques have been proposed to expedite convergence and pseudo-time marching of the resulting problem (e.g., [83]).

To solve the Darcy-Brinkman equation for the flow field, we employ a Two Relaxation Time (TRT) model as proposed by [84], and the classical TRT collision scheme for advection-diffusion [85], implemented in [86] for the transport equation. The TRT scheme used in this work belongs to a family of Brinkman-forcing-based methods, in contrast to lattice Boltzmann methods based on 'partial bounce-back'. In the former, the friction related to the presence of the porous medium is modeled using modified collision terms that mimic the bounce-back rules typically used at solid boundaries, hence the name. In Brinkman-forcing methods, the mass force term is explicitly used in a collision kernel. This approach was chosen because it has a clearer connection with the partial differential equations describing dissolution at the Darcy scale and provides an explicit link between porosity and permeability evolution and the flow.

In this work, we use the D3Q19 lattice model for 3D and the D2Q9 lattice model for 2D, as described in [87], in a simplified version without making use of the recurrence relations. This model has been successfully applied to numerous porous media-related problems, particularly for the calculation of the flow field from μ-CT imaging data in [88]. We follow the models provided therein, but define them in pseudo-time and implement the collision in moment space, which is then mapped back to distribution space for streaming. Additional details of the method are provided in Appendix A

3 Test cases

Several test cases were considered for validation of the proposed numerical method and assessment of its accuracy. We started with simple 1D cases designed to test different elements of the model, moving next to more sophisticated 2D and 3D systems, in which the instabilities develop. Additionally, preliminary performance data for large-scale 3D cases have been obtained on two HPC systems. All parameters used in simulations are summarized in Table 1. We use LBM units here, defined by the lattice spacing, δx and LBM time step, δt.

3.1 Non-uniform 1D permeability

To validate the Darcy-Brinkman model underlying the flow solver, a simple test case was designed. In the 2D domain with dimensions $L_x \times L_y$, a random porosity field was initialized, which varies only in the direction of

Table 1 Simulation parameters for all the cases described in the article. We use LBM units here, defined by the lattice spacing, δx and LBM time step, δt

Parameter	Symbol	Section 3.1	Section 3.2	Section 3.3	Section 3.4	Section 3.5
Kinematic viscosity,	ν/ρ	1/6	1/6	1/6	1/6	1/6
Diffusion constant	D	–	0.002	0.002	0.008	0.008
Average Darcy velocity	u_0	0.01	0.02	0.01	0.015	0.015
Specific reaction area	s_0	1	1	1	1	1
Dissolution time step	$\Delta t/t_d$	–	–	0.8	0.8	0.8
Reaction rate	r_0	–	0.002	0.002	0.002	0.002
Magic relaxation rate	Λ	4/8	1/12	1/12	1/12	1/12
Grid size ($L_x \times L_y$)	–	224 x 32	128 x 16	256 x 16	512 x 256	512 x 256
# of iterations per time-step	–	–	–	–	0.5 to $8L_x/u_0$	L_x/u_0
Initial porosity	φ_0	–	0.5	0.5	(0.015,0.85)	(0.015,0.85)
Permeability	κ	(0.05,0.1)	(0.05,0.1)	(0.5; 1)	$\left(4 \times 10^{-6}; 28\right)$	$\left(4 \times 10^{-6}; 28\right)$

Fig. 1 Schematic of a 2D domain used in the permeability convergence test. Colors indicate local variations in porosity and permeability. In the context of Darcy-Brinkman flow, the steady solution corresponds to uniform flow. However, achieving such a solution takes place only after a (pseudo)time τ_r due to the compressibility effects of the LBM

the flow:

$$\varphi(x, y) = \varphi_0(x), \tag{15}$$

(see Fig. 1). With a constant flow rate, u_0, imposed at the inlet, this case has a trivial uniform solution, $u(x, t) = u_0$, throughout the entire domain. However, due to the numerical compressibility effects of LBM, a certain number of iterations are needed for the system to reach a steady state.

The convergence time, assessed in this manner, can be used to estimate the number of pseudo-time steps of the LBM method that need to be performed between the global time steps. The results of this analysis are summarized in Fig. 2. For the set of parameters used, the deviation $|{<u>}/u_0-1|$ becomes smaller than 10^{-3} for $t_R \approx 13L_x/u_0$, which is later used as an estimate for the number of iterations needed between global time steps (porosity updates) in transient simulations.

3.2 Concentration profile within a reactive solid

The evaluation of the reactive transport model was performed using the same permeability distribution and boundary conditions as in the previous section, with a constant reactive surface area, $s_0 = 1$. In such a case, the steady-state transport Eq. 2 can be solved explicitly to yield:

$$c(x) = c_0 \exp\left(-x/\lambda\right), \tag{16}$$

with the penetration length:

$$\lambda = \frac{2D}{\sqrt{u_0^2 + 4s_0 D} - u_0}. \tag{17}$$

The variable permeability field was included to monitor any effects of the variable Brinkman force term and variable pressure drop on simulation results. The analytical solution for the velocity field should correspond to a constant velocity ($u = u_0$) throughout the entire domain.

Fig. 2 Left: porosity profile in permeability convergence test system. Right: Relative error $|{<u>}/u_0 - 1|$ as a function of pseudo-time

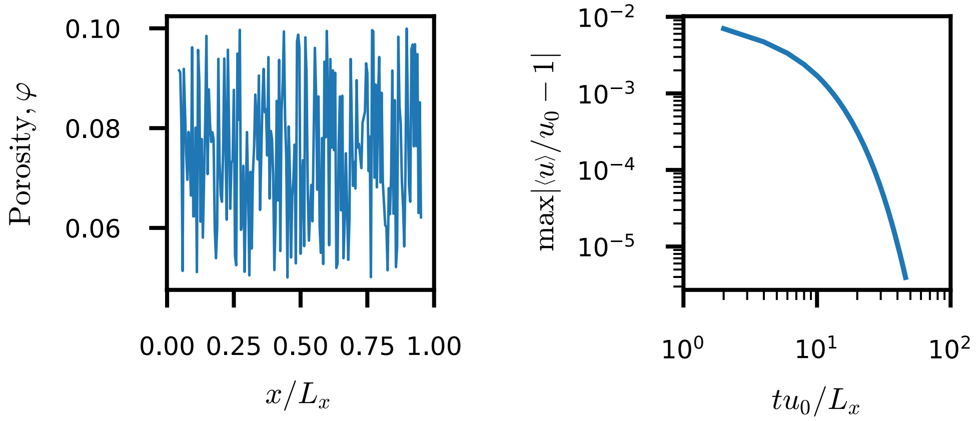

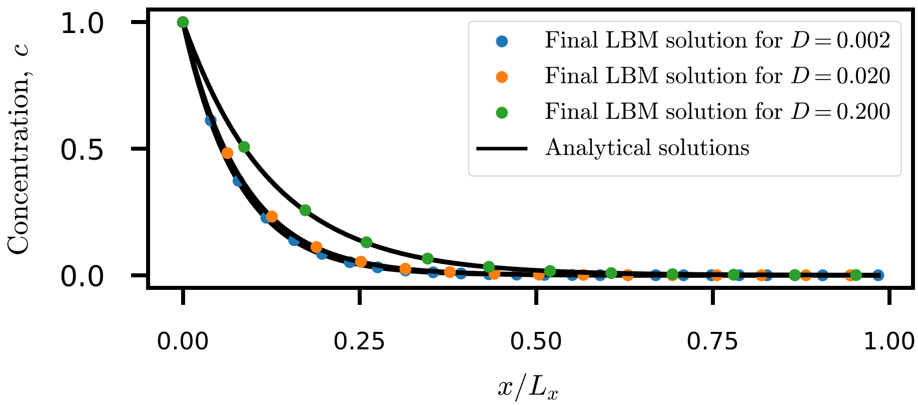

Fig. 3 The concentration profile inside a reactive porous medium. Simulation results (red dots) compared with the analytical solution (16) (black solid line)

Figure 3 presents the comparison between the analytical solution (16) and the converged LBM solution. It should be noted that LBM methods become unstable as D approaches zero. Therefore, the presented solution is calculated for $Pe = \frac{u_0 L_x}{D} = 640$, which corresponds to $D = 0.002$. The close match with the theoretical solution demonstrates the solver's accuracy for reactive-flow calculations and confirms the proper implementation of the outlet boundary condition.

3.3 Reactive front propagation

In this section, we utilize a 1D porosity field with the initial porosity $\varphi_0 = 0.5$ as a benchmark case. This time, we will let the porosity evolve according to Eq. 3, assuming the sugar-lump model (6) for the specific reactive area.

In the long-time limit, such a system approaches a travelling-wave solution, closely related to the dissolution and dissolution–precipitation fronts analysed in one-dimensional reactive–transport models for porous media, where the front speed and internal structure are set by the balance of advection, dispersion and reaction [89–91].

In such case, c and φ become functions of $x' = x - Vt$, where V is the reactive front velocity. The latter can be derived from mass conservation [81]. Per unit time and unit area, $u_0 c_0$ moles of reactant are entering the system. Each mole dissolves the mineral volume of $\nu \mathrm{v}_m$, corresponding to the rock volume of $\nu \mathrm{v}_m/(1 - \varphi_0)$. Thus:

$$V = c_0 u_0 \frac{\nu \mathrm{v}_m}{1 - \varphi_0}. \tag{18}$$

In the above derivation, we assumed that the solute concentration c_0 is much smaller than mineral concentrations, v_m^{-1}, hence the reactive front velocity is much smaller than the average flow rate, u_0. In the frame moving with velocity V, the erosion equation becomes [71]:

$$\frac{\partial \varphi}{\partial t} - V \frac{\partial \varphi}{\partial x'} = \nu \mathrm{v}_m R(c, \varphi), \tag{19}$$

with the boundary condition, $\varphi(-\infty) = \varphi_0$. On the other hand, the steady-state transport equation retains the same form as in the LAB frame:

$$u_0 \frac{\partial c}{\partial x'} = -R(c, \varphi), \tag{20}$$

with the boundary condition $c(-\infty) = c_0$, corresponding to the incoming solution. The traveling wave solution can then be obtained by dropping the time-dependent term in Eq. 19 and solving the resulting ordinary differential equations.

In Fig. 4, the propagating solution obtained by the LBM solver is presented for the domain discretized into 256 lattice points. The traveling wave is shown around the center of the domain, where the boundary effects are minimal. In Fig. 5, we verify the LBM concentration and porosity profiles against a direct integration of the

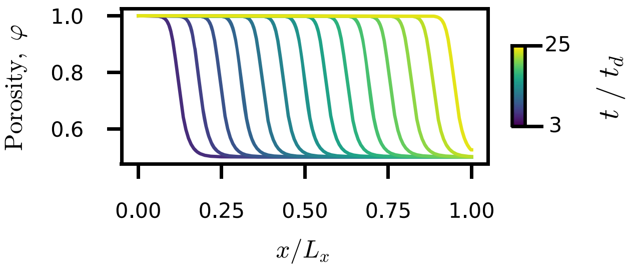

Fig. 4 Travelling wave solution: evolving porosity profile emerging during the dissolution of an initially uniform system. Different curve colors correspond to different times

steady-state form of Eqs. 19-20. Two different integration methods were used to obtain reference solutions. The first one uses the LSODA procedure from ODEPACK [92] and the second uses the 3(2) order Runge-Kutta RK23 method [93], both implemented in the SciPy library. The LBM code relies on second-order implicit integration with a fixed time step, while both ODE solvers have error-controlled time step sizes. A certain mismatch can be seen between the LBM and 4/5th-order LSODA solution, which can be attributed to an insufficient order of integration of the LBM method. As already mentioned, our model has a non-smooth RHS as it approaches $\varphi = 1$. While the LSODA package implements stiffness handling and order switching, the RK23 does not. The solution obtained using the former implementation has been included to illustrate the numerical oscillations exhibited by a scheme without proper handling of the piece-wise continuous RHS of Eq. 19.

3.4 2D wormhole growth, global mass conservation

One of the main reasons for the development of our solver was to conduct wormhole simulations in a highly heterogeneous porosity field. To test the performance of the method in such a setting, we evaluated it for a non-correlated random porosity field sampled uniformly from the interval $(0.15, 0.85)$, while the Carman-Kozeny coefficient was set at $\kappa_0 = 1$. The average initial porosity is $\varphi_0 = 0.65$, which corresponds to the specific surface area per unit volume $s = 4s_0\varphi_0(1-\varphi_0) = 0.91$, for $s_0 = 1$. The Péclet number and Damköhler numbers were equal to 3.16 and 64 respectively, which corresponds to the wormholing regime in the morphological phase diagram.

Figure 6 presents the porosity, concentration, and flow field at four different moments in time, as obtained from the simulations. One can clearly observe the formation of wormholes originating from the initial porosity inhomogeneities and their subsequent progression into the medium. As the channels grow, they compete with each other for available flow and reactant flux, resulting in the faster growth of longer channels at the expense of their neighbors. This phenomenon aligns with previous observations [2, 94], where the range of interaction between the channels increases proportionally to their length. Consequently, a single dominant wormhole eventually emerges, concentrating the entire flow, as depicted in Fig. 6.

One important property of the Darcy-Brinkman model is the transition from Darcy to Stokes flow as permeability increases. To verify that this transition occurs within the dissolution channels, we have analyzed the evolution of flow profiles in this region. As depicted in Fig. 7, an initially random velocity field transforms into parabolic profiles within the fingers, which is a characteristic of Stokes flow. The left profile corresponds to the dominant

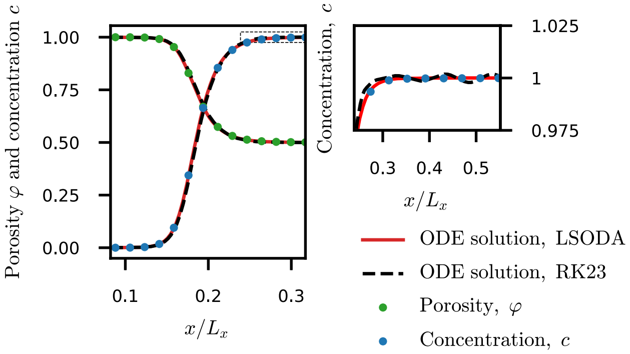

Fig. 5 Porosity and concentration profiles in the travelling wave solution obtained from the LBM (circles) and by a direct solution of the differential equations (19)-(20) in a co-moving frame (solid lines). Two different methods were used to integrate ODE: Runge-Kutta 2/3 (RK23) and Adams/BDF LSODA. In the inset, instabilities in the RK23 method are visible, while both LSODA and the LBM implementation remain stable. This behaviour is triggered by lack of smoothness of RHS, not handled in RK2/3 implementation

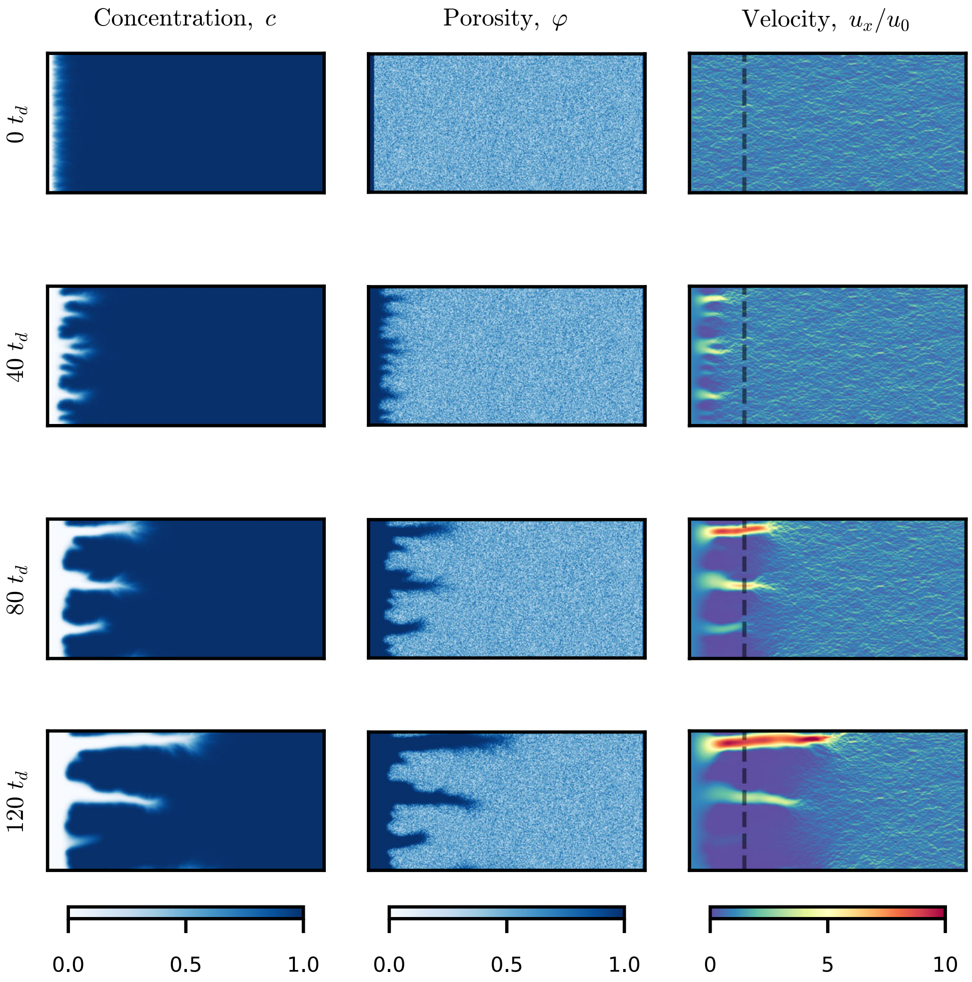

Fig. 6 Wormhole evolution in a random porosity field. The dashed line denotes the cross-section for which the velocity field is plotted in Fig. 7

finger, while the right one corresponds to the second-longest finger, which gradually loses volumetric flux to the dominant finger.

Dissolution codes are particularly susceptible to problems related to global mass conservation, with discrepancies typically accumulating over time. In fact, the difference between the reactant flux entering and leaving the system must be balanced by global porosity change per unit time:

$$\Delta_m(t, \delta t) = (J_{in} - J_{out})\delta t - \frac{1}{\nu v_m} \int \delta\varphi(\mathbf{r}, \delta t) d\mathbf{r}. \tag{21}$$

Here, J_{in} and J_{out} represent the total incoming and outgoing flux, respectively, and $\Delta_m(t, \delta t)$ is the mass conservation error, ideally zero. Although the Lattice Boltzmann Method (LBM) is a conservative approach, it is weakly

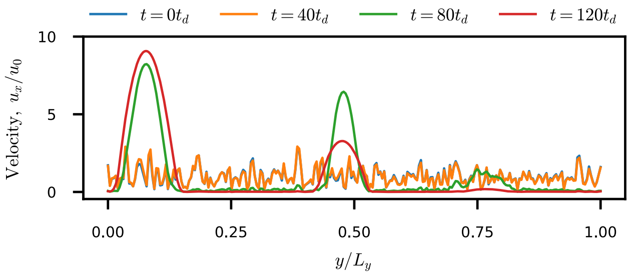

Fig. 7 Time evolution of the velocity field at the cross-section marked in Fig. 6. A clear transition from a Darcy profile to a parabolic one is visible inside the wormholes, enhanced by the flow focusing in the dissolved channels

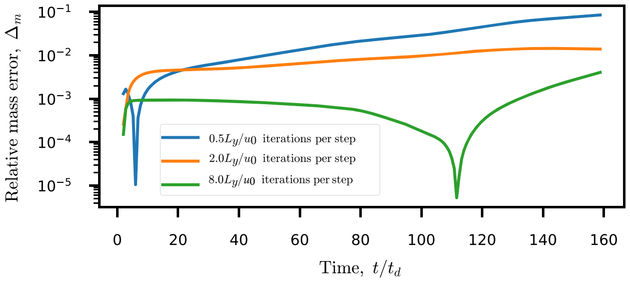

Fig. 8 Total mass conservation error, Δ_m (21), as a function of time t. This error can be reduced by increasing the number of pseudo-time steps of the LBM code performed between global update steps. If both velocity u_0 and domain length, L_y, are expressed in LBM units then advective time scale L_y/u_0 can be used as a reference for the number of internal iterations. See Section 3.1 for details

compressible, meaning $\nabla \cdot \mathbf{u} = \epsilon$, where ϵ is a numerical (preferably small) compressibility error. This error can be significantly reduced by increasing the number of pseudo-time steps per global update, as illustrated in Fig. 8. In different solution methods where linear equations need to be iterated (for instance, derived from finite difference formulations), this is equivalent to performing a higher number of iterations of the linear solver.

3.5 Resolution impact on wormhole evolution

The primary motivation for this work is to explore the capabilities of next-generation supercomputers in simulating wormhole evolution at a resolution sufficient to capture the growth dynamics at the laboratory sample scale. The underlying question here pertains to the scale dependence of wormhole evolution. In other words, we aim to determine whether there is a scale at which Darcy-Brinkman-type simulations can recover instability growth with enough detail to capture global statistics, or whether the Darcy-based model is fundamentally insufficient to study such processes in natural heterogeneous media.

To assess changes in geometric properties of the wormhole, such as tortuosity, in response to the resolution of the underlying porosity data, we generated a high-resolution parent initial porosity field with a prescribed correlation length and used its downsampled versions as lower-resolution input.

The initial porosity field is sampled a lognormal distribution $\ln \varphi(x, y) = b + \psi(x, y)$ where $\psi(x, y)$ is a Gaussian random field with an exponential covariance function of the following form

$$\langle \psi(x, y)\psi(x + \Delta x, y + \Delta y)\rangle = \nu^2 \exp\left[-\frac{\sqrt{\Delta x^2 + \Delta y^2}}{l_c}\right],$$

with spatial autocorrelation length l_c. Since porosity is limited by 1, we need to truncate the longnormal distribution from above, the formulas linking the first and second moment of such a distribution with the parameters of the underlying normal field can be found e.g. in [95]. The distributions with desired mean ($\langle \varphi \rangle = 0.106$), standard deviation ($\sigma = 0.5$) and correlation length ($l_c = 3\delta x$) were generated using Fourier filtering method [96].

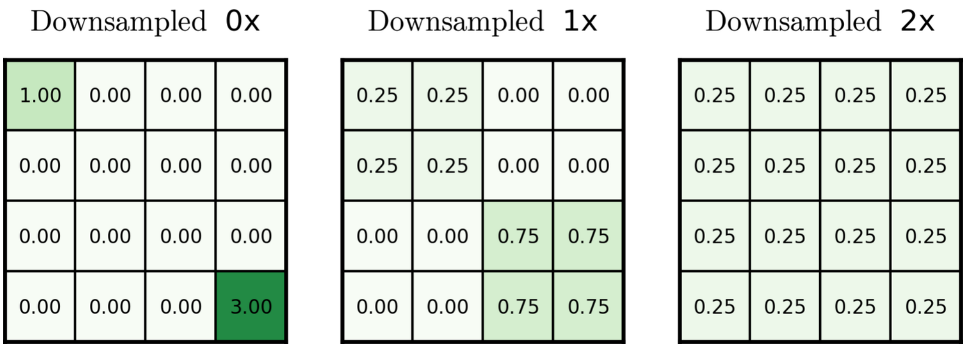

Downsampled 0x

1.00	0.00	0.00	0.00
0.00	0.00	0.00	0.00
0.00	0.00	0.00	0.00
0.00	0.00	0.00	3.00

Downsampled 1x

0.25	0.25	0.00	0.00
0.25	0.25	0.00	0.00
0.00	0.00	0.75	0.75
0.00	0.00	0.75	0.75

Downsampled 2x

0.25	0.25	0.25	0.25
0.25	0.25	0.25	0.25
0.25	0.25	0.25	0.25
0.25	0.25	0.25	0.25

Fig. 9 Down-sampling and resizing process illustrated on 4x4 grid

Subsequently, dissolution simulations were performed with varying down-sampling rates of the porosity field while preserving full resolution for the flow calculations. Down-sampling involved the arithmetic averaging of surrounding nodes. To maintain the original flow field simulation resolution, the final dataset was expanded back to its original size as a piece-wise constant function. The downsampling process is illustrated on a 4x4 array in Fig. 9. For better statistical representation, the simulation was repeated with 40 different realizations of the porosity field.

In Figs. 10 and 11, the evolution of porosity and wormhole skeletons during dissolution is presented at different resolutions for the same realization of a random porosity field. It is evident that as the resolution of the porosity field decreases, small-scale features of the wormhole disappear. Furthermore, downsampling by more than four times (effectively by a scale factor of 2^4 or larger) noticeably alters the geometry of the dissolution finger. Branchings appear in other time moments and spatial positions, and a different finger grows the fastest compared to less downsampled cases. Eventually, for 7 or more downsamplings, the fingers become straight - most of the information about the smaller-scale details in the porosity field is lost at this point. This behavior is likely the result of the interplay between the length scale associated with wormhole evolution (dependent on Péclet and Damköhler numbers) and the characteristic length scale of the porosity field, specifically the correlation length. The loss of spatial heterogeneity is also observable when calculating the autocorrelation function (ACF) of the initial porosity field

$$\mathrm{ACF}(\varphi) \equiv \frac{\langle(\varphi(\mathbf{r})-\varphi_0)(\varphi(\mathbf{r}+\mathbf{l})-\varphi_0)\rangle_{\mathbf{r}}}{\langle(\varphi(\mathbf{r})-\varphi_0)^2\rangle_{\mathbf{r}}}, \tag{22}$$

where $\varphi_0 = \langle\varphi\rangle_{\mathbf{r}}$ is the mean value of porosity and $\langle\ldots\rangle_{\mathbf{r}}$ denotes averaging over $\mathbf{r}$. In Fig. 12, ACF calculated based on 40 different realizations of the initial porosity field is presented, along with an estimate of the characteristic length, l_{90}, over which the correlations decay. In analogy to boundary layer theory, we define l_{90} as the point

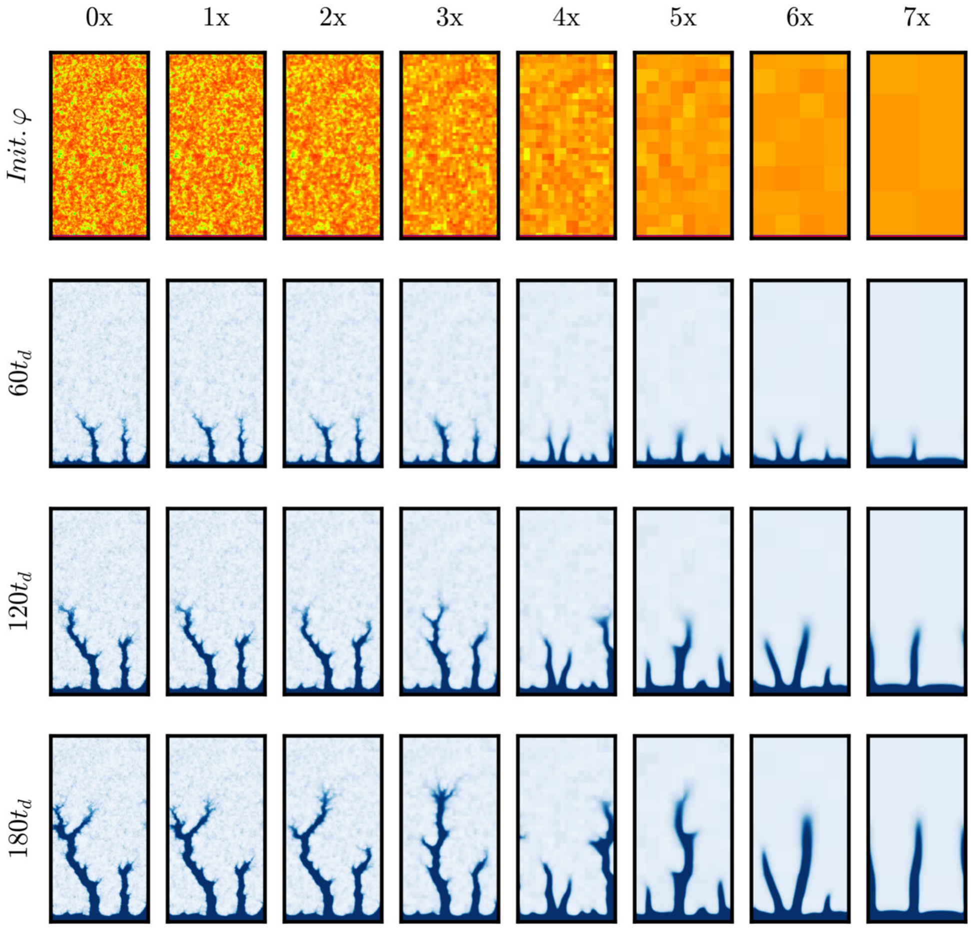

Fig. 10 Porosity field evolution during dissolution (from top to bottom) of the same initial random field, which was downsampled (from left to right: the original field, and fields obtained by the application of n-fold downsampling procedure with n=1 to 7)

Fig. 11 Skeletonized structures of dissolution wormholes at $t = 180t_d$. The numbers indicate the degree of downsampling of the initial porosity field

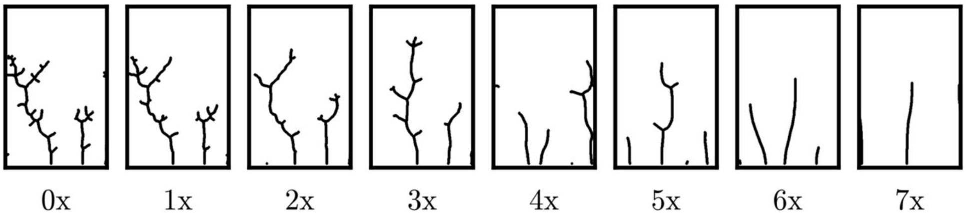

for which ACF($\mathbf{r}$) drops below 0.1. Such a definition of a correlation length is preferred over the estimate of an exponential decay length of ACF(φ) because for larger down-sampling rates, the ACF($\mathbf{r}$) loses its exponential character and becomes a piecewise linear function in $\mathbf{r}$. One can observe that while a single down-sampling has a negligible effect on the spatial properties of the random field, changes become significant beyond a threefold reduction, which is consistent with the fact that initial field was created with correlation length equal $3\delta x$.

Such a loss of correlation with downsampling is consistent with the observations of Ref. [97], which emphasized the need for high-resolution data in reactive flow simulations. Additionally, the impact of the porosity field correlation length on dissolution patterns has been recognized by several researchers [11, 60–64], who specifically noted that it controls the branching rate at the wormhole tip as well as the distance between neighboring branches. This is fully consistent with the observations made from Fig. 10, clearly showing less ramified structures with increasing downsampling (which, according to Fig. 12, leads to an increase in correlation length).

Another way to quantify the changes of the dissolution patterns with downsampling is by calculating the transversely averaged porosity profiles, analogous to the characterization of miscible fingering in porous media in terms of transversely averaged concentration profiles [98, 99].

$$\chi(x) = \frac{1}{L_y} \int_y \frac{\varphi(x, y) - \varphi_0}{1 - \varphi_0} dy, \tag{23}$$

where we also average over realizations. The profiles are presented in Fig. 13. As we observe, the first few profiles overlap, showing that the differences between the wormholes are relatively minor and limited to small-scale features. Only after 4-fold downsampling do the profiles begin to diverge, generally showing more dissolution at smaller x and a much less developed large-x tail in the $\chi(x)$ dependence. This is consistent with the wormhole morphologies observed in Fig. 10, where larger downsampling rates result in shorter, bulkier, and less branched wormholes, as well as a more extensive fully dissolved region near the inlet.

Yet another way of quantifying the resolution effect is to calculate the tortuosity of the wormholes and compare it across different resolutions. The tortuosity of the wormhole, τ, is defined here as the total length of a flowpath starting at the wormhole root and finishing at its tip, divided by the extent of the wormhole along the x (flow)

Fig. 12 Left: The porosity autocorrelation function ACF(l) (22) at different downsamplings of the initial porosity field, averaged over 40 realizations. Right: A characteristic decay length, l_{90}, of ACF(l) defined as the point for which ACF drops below 0.1 (as marked by the black dots on the left panel)

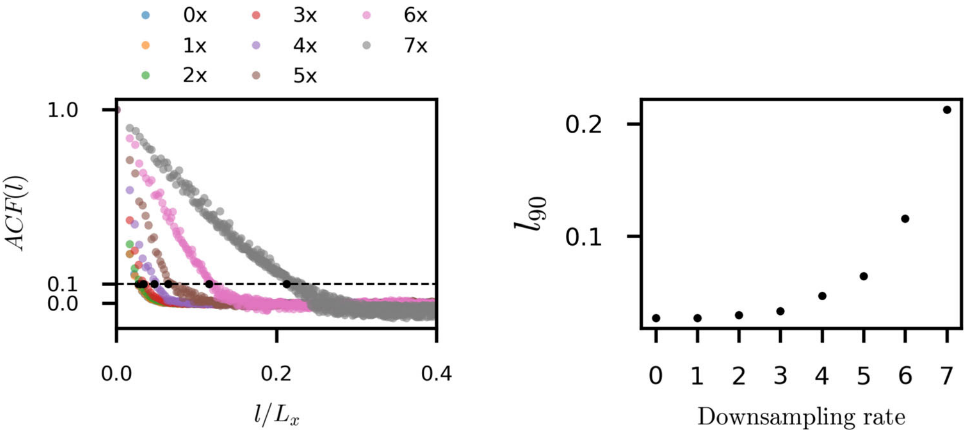

Fig. 13 Left: transversely-averaged porosity profiles, $\chi(x)$ for $t = 120t_d$ averaged over 40 realizations of the initial porosity field. Right: A magnification of the region of the $\chi(x)$ graph marked by the dotted rectangle in the left panel

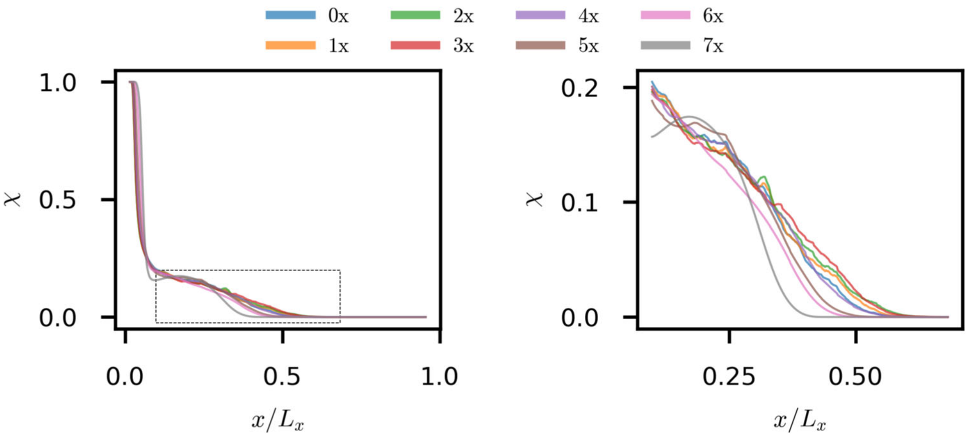

direction. The dependence of the tortuosity of the longest wormhole on the resolution is presented in Fig. 14. Similar to the ACF, there are no significant changes between the original sample and one-fold or two-fold reductions in resolution, with larger changes taking place beyond a 3-4 fold reduction. This indicates that the correlation length of the porous matrix plays a crucial role in wormhole development, and it is important to examine the influence of planned down-sampling on the correlation of simulation data.

In the analysis above regarding the influence of downsampling on wormhole patterns, we were coarse-graining the initial porosity field while always keeping the computational grid the same (512x256 in the simulations illustrated in Fig. 10). From a practical viewpoint, this corresponds to a situation where we have sufficient computational resources but are limited by the resolution of the experimental apparatus. As we have shown, in such a situation, the predictions of our reactive transport models can be seriously compromised.

However, we often encounter a situation where we are in possession of high-resolution data on the porosity field (e.g., from tomographic imaging), but due to the overall size of the experimental system, we are unable to run the simulations at full resolution. In such cases, to reduce the computational cost, one often reduces the resolution of the computational grid, which entails a simultaneous downscaling of the initial porosity field.

Fig. 14 Average tortuosity versus time at different downsamplings of the initial porosity field, averaged over 40 realizations. Tortuosity was first normalized by that of a non-downsampled case, and then averaged over both time and different realizations. The average standard deviation over time and between realizations is also presented

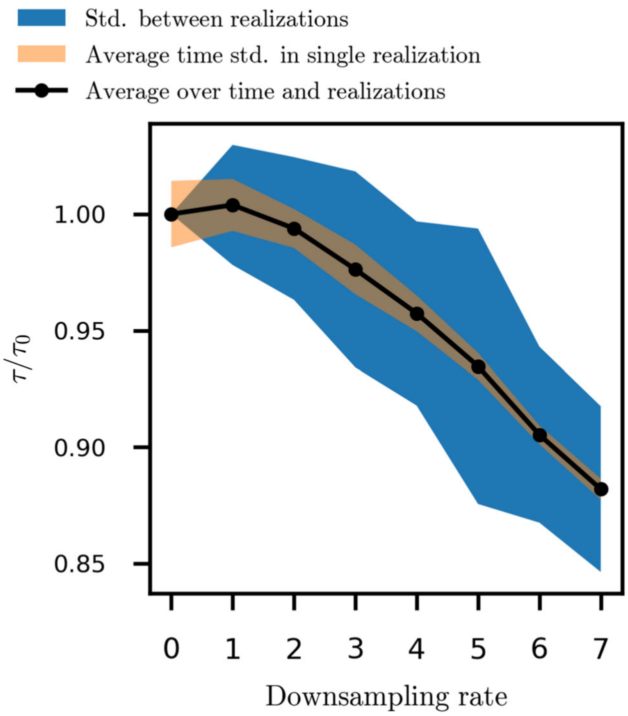

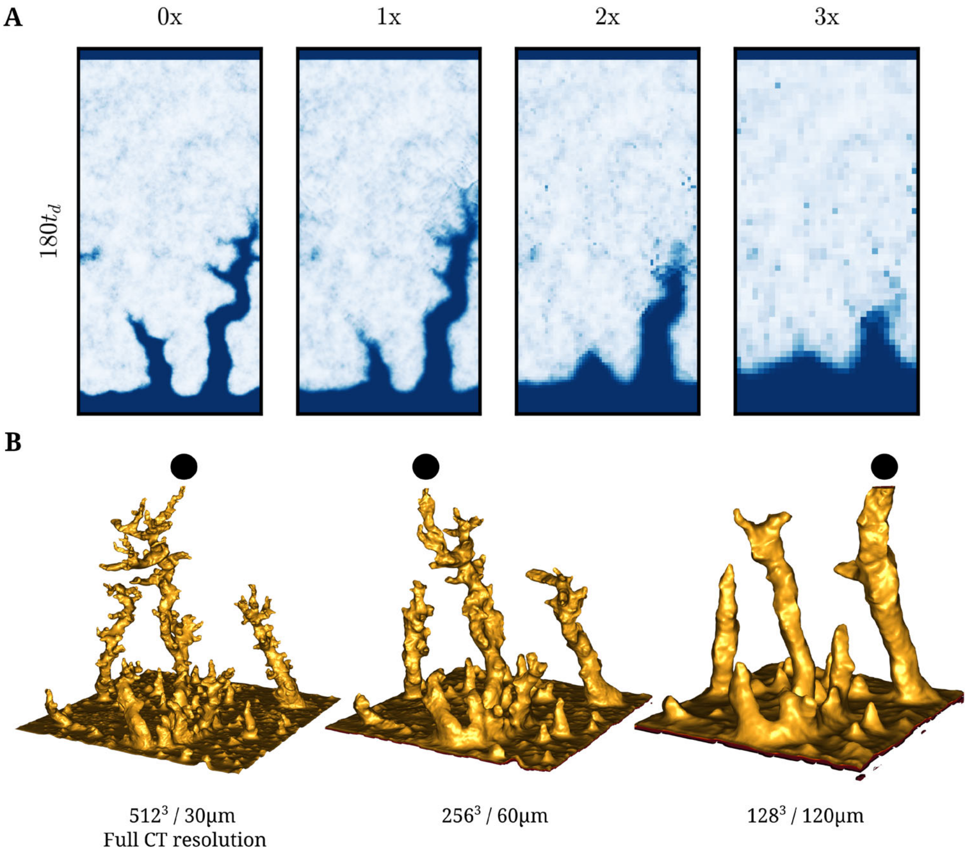

Fig. 15 Simultaneous downsampling of both the input porosity field and the underlying computational grid has a stronger effect than sole porosity downsampling. **A** illustrates such downsampling on synthetic 2D data, similarly to Fig. 10. **B** illustrates the effect of downsampling on acidization simulation of Pińczów limestone based on tomographic data taken from Cooper et al. [65]. A black dot denotes the dominating channel

Such an approach is illustrated in Fig. 15A. As we see, the use of a coarse computational grid dramatically affects the appearance of dissolution patterns, much more than the downsampling effects on the initial porosity fields. In this case, already at 3x downsampling, the wormholes are basically gone, and the instability is considerably reduced.

These aspects need to be kept in mind when analyzing data on real rocks. The porosity correlation length of the rocks is of the order of 50-200μm [100], which means that for the wormholing to be faithfully reproduced, the resolutions of the initial porosity field should be in the range of 10-60μm. Such resolutions can be obtained using X-ray microtomography [36, 65, 101, 102]. Preferably, the computational mesh should be of comparable size. As an example, in Fig. 15B, we present the patterns obtained based on the simulation of dissolution of a porosity field of approximately 1cm^3 of Pińczów limestone, on which the dissolution experiments have been performed [65].

For the three-dimensional Pińczów limestone example, the initial porosity field is constructed directly from a high-resolution X-ray μCT scan. The greyscale image is segmented into three phases (solid grains, macropores and an intermediate microporous phase), following the three-phase segmentation approach used for carbonate rocks by Luquot et al. [29]. This segmentation yields a voxel-wise porosity field taking values between 0 and 1. At coarser resolutions, porosity on the Darcy–Brinkman grid is obtained by simple volume averaging of the underlying voxels. Permeability is then computed from this porosity via a Carman–Kozeny–type relation. In this work, the 3D case is used primarily to demonstrate the feasibility and performance of large-scale simulations on realistic porosity fields, rather than to provide a fully calibrated prediction for a specific core.

The simulations performed at the resolution of the tomographic data (30 μm) show highly ramified wormholes with a large number of small branches. As we decrease the computational resolution to 60μm, not only is this level of detail significantly reduced, but also a different branch dominates the growth. Finally, at the resolution of 120μm, the wormholes become straighter and thicker with just a couple of short side-branches.

Keeping such a high resolution is computationally demanding, given the size of the experimental systems (which is usually in the 1-10 centimeter range along each dimension). This is why the question of performance and numerical efficiency is key here. This is where LBM methods, which are highly parallelizable and possible to run on GPU clusters, show their real strength. We will look more closely into these matters in the next section.

4 Performance evaluation

The 3D variant of the solver was evaluated on NVIDIA V100 and AMD MI250X cards. Benchmarks were conducted on the Rysy cluster at the Interdisciplinary Centre for Mathematical and Computational Modelling at the University of Warsaw and on the petascale LUMI supercomputer at the CSC data center in Kajaani, Finland, during its pilot phase (in late 2022). It is worth noting that there are significant architectural differences between these clusters, including their size. Rysy consists of seven nodes, while LUMI is a Cray system built from thousands of nodes. On the other hand, NVIDIA's software stack for GPU development is well-established and stable, whereas AMD's software stack is still under development, and its accelerators are not yet widely available. Since many newly installed systems in the TOP500 list are based on AMD and NVIDIA solutions, we consider it worthwhile to discuss the performance data for both types. However, these results should only be considered indicative, given the differences between the two HPC systems. The aim of this section is to provide an overall estimate of the expected system size that can reasonably be resolved with the available resources. As MI250X accelerators have been available since 2022 in several large HPC installations, performance improvements are anticipated, as both the HIP software stack and the TCLB codes are tuned for maximum performance on this relatively new architecture. During the benchmarks, a slightly different collision scheme was used for the 3D reactive-transport component, specifically the central-moments relaxation scheme (as implemented in [86]), because a stable version of the TRT implementation was not available during the pilot phase on the LUMI system. Only minor performance differences are expected between the TRT and central-moments formulations for this kind of simulation, resulting only from a slightly different number of arithmetic operations in the collision operator.

Benchmark results for both systems and three system sizes (20, 134, and 697 million voxels) are summarized in Fig. 16. TCLB was able to achieve 120 GLBUps (10^9 lattice block updates per second) using 1024 MI250X cards. However, the declared peak double precision performance of those cards is around 48 TFLOPs, whereas the V100

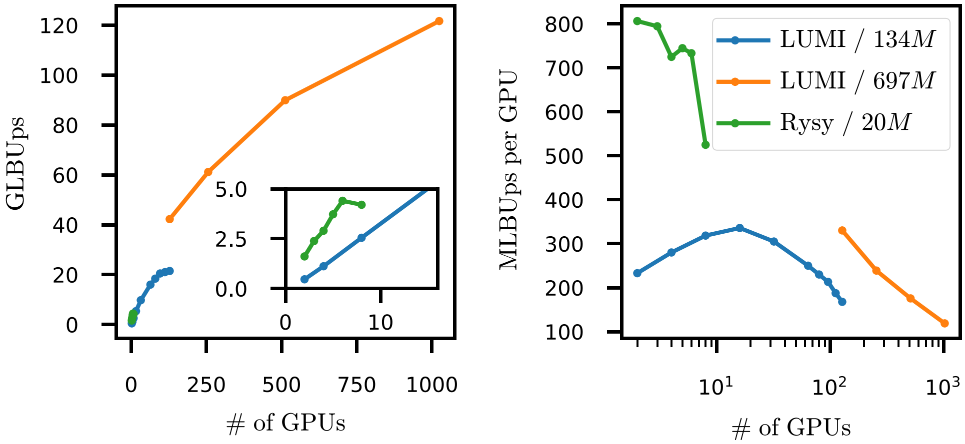

Fig. 16 Iteration speed, in million lattice blocks updated per second (MLBUps), is shown for various lattice sizes (ranging from 20×10^6 to 700×10^6) on two different HPC systems: the Rysy cluster at ICM UW in Poland and the LUMI supercomputer at CSC in Finland. Both the speedup (left) and the strong scaling (right) are presented. Note that the evaluation on the LUMI system was conducted during the pilot phase in late 2022, and achieving the full system performance on MI250X accelerators was likely not possible. The TCLB code was originally designed for NVIDIA GPUs but is expected to improve over time on AMD hardware as well

card is declared to have 8 TFLOPs. The single-card performance measured on MI250X cards was below 50% of the V100 speed, indicating that a speedup of almost an order of magnitude might be possible. This would correspond to an iterative performance of 10^{12} LBUps with 1024 cards in use. Such scaling properties could potentially allow dissolution simulations of 10 cm-scale cores at a resolution of a few micrometres using only 10% of the LUMI cluster, and such job sizes are already available for standard users. Furthermore, ML-based preconditioners for porous media flows are reported to provide even 10× faster convergence for steady-state LBM simulations [103].

In summary, even at the Darcy–Brinkman scale, the combination of core-scale domain sizes and micrometre-scale resolution places these simulations close to current computational limits. A fully pore-scale direct numerical simulation of a core of comparable size would exceed available memory and CPU budgets by several orders of magnitude, which further justifies the mesoscopic Darcy–Brinkman approach adopted here.

5 Summary

In this work, we have introduced an efficient and highly parallelizable numerical approach for simulating reactive flow in dissolving porous media, based on the lattice Boltzmann method. While a number of different reactive-flow solvers exist, we have built on recent advancements in the lattice Boltzmann method to achieve additional stability and performance improvements. The numerical approach incorporates the TRT collision scheme for both the concentration transport equation and the momentum equation. Furthermore, the TRT formulation for the Darcy–Brinkman problem is a collision variant designed to minimize artifacts that may arise in highly non-uniform porosity fields. This is especially crucial for accurately representing flow and transport near the boundaries of growing wormholes, voids, or low-permeability regions within the system. When combined with the utilization of pre-exascale and exascale computers like LUMI, this approach makes it possible to conduct dissolution simulations in laboratory-scale systems (a few centimeters in size) with a resolution of approximately 10–30 μm. Our study has examined the development of reactive-infiltration instabilities in heterogeneous media and elucidated the critical relationship between the spatial resolution of structural data and the accuracy of simulation outcomes. In particular, we have highlighted the existence of a minimum resolution necessary for simulations to authentically represent the geometric intricacies of dissolution channels. At resolutions below this threshold, we observed a pronounced simplification of channel morphology—channels became straighter, more bulky, and less intricately branched, diverging from their natural counterparts. Thus, any predictive simulation of dissolution experiments will necessarily be computationally intensive, making a natural case for high-performance computing and highly parallelizable codes like LBM in these endeavors.

Appendix A: Lattice Boltzmann scheme

As in all LBM models, the explicit update rule for the flow field is given by

$$f_i^{k+1}(\mathbf{x}_\alpha + \mathbf{e}_i) = f_i^k(\mathbf{x}_\alpha) - \left(\Lambda^+ + \frac{1}{2}\right)^{-1} \left(f_i^+ - f_i^{eq,+} - \Lambda^+ F_i^+\right) - \left(\Lambda^- + \frac{1}{2}\right)^{-1} \left(f_i^- - f_i^{eq,-} - \Lambda^- F_i^-\right),$$

where $f_i^k(\mathbf{x}_\alpha)$, or f_i^k for brevity, denotes the i-th particle distribution function (PDF) defined at the point $\mathbf{x}_\alpha$ at iteration k. The point $\mathbf{x}_\alpha$ belongs to an evenly spaced Cartesian grid (lattice). The vector $\mathbf{e}_i$ is a connection vector, connecting two neighbouring grid points in direction i. f_i^{eq} denotes the LBM equilibrium distribution function, and Λ is the relaxation rate. The plus and minus superscripts indicate the symmetric and antisymmetric components of a given quantity q, defined as

$$q_i^+ = \frac{1}{2}(q_i + q_{-i}), \tag{A.1}$$

$$q_i^- = \frac{1}{2}(q_i - q_{-i}), \tag{A.2}$$

where $\mathbf{e}_{-i} = -\mathbf{e}_i$. From a performance perspective, it is convenient to evaluate the LBM scheme in a chosen moment space, where a single raw moment m_j is defined as

$$m_j = \sum_i f_i \left(e_{i,x}\right)^p \left(e_{i,y}\right)^q \left(e_{i,z}\right)^r . \tag{A.3}$$

For the TRT scheme with an odd–even split, the odd and even moments can be identified with the + and − components (see also [86])

$$m_j^{even} = \begin{cases} \sum_i \left[f_i \left(e_{i,x}\right)^p \left(e_{i,y}\right)^q \left(e_{i,z}\right)^r\right] = m_j^+ & p+q+r = 2n, \\ 0 & p+q+r = 2n+1, \end{cases}$$

$$m_j^{odd} = \begin{cases} 0 & p+q+r = 2n, \\ \sum_i \left[f_i \left(e_{i,x}\right)^p \left(e_{i,y}\right)^q \left(e_{i,z}\right)^r\right] = m_j^- & p+q+r = 2n+1, \end{cases}$$

and the vector of moments is then given by

$$m_j = m_j^{even} + m_j^{odd}.$$

Multiplying the evolution equation by the raw-moments generating matrix M yields the evolution equation in the form

$$f_i^{k+1}(\mathbf{x} + \mathbf{e}_i) = M_{ij}^{-1} \left\{ m_j - \left(\Lambda_j + \frac{1}{2}\right)^{-1} \left(m_j - m_j^{eq} - \Lambda F_j\right) \right\}.$$

The Magic relaxation factor Λ is defined as

$$\Lambda_j = \begin{cases} \Lambda^+ = \frac{9(4+B)\nu_e}{4(3+2B\Lambda)} & \text{for even moments,} \\ \Lambda^- = \frac{\Lambda}{3\nu_e} & \text{for odd moments,} \end{cases} \tag{A.4}$$

where the effective viscosity ν_e is equal to $\frac{\nu}{f}$, while the parameter $B = f/\kappa$. Following the assumption $\nu = \nu_e$ we set $f = 1$. This relation between the relaxation parameters and the permeability ensures a uniform effective viscosity in a variable-permeability field [87]. It should be highlighted that both the effective viscosity and the parameter B might, in principle, depend on the friction term and therefore $f = f(\varphi)$. For the complete Darcy–Brinkman equation, the force term is introduced via the source term

$$F_j = M_{ij} \left(\frac{w_i \mathbf{e}_i}{c_s^2}\right) \left(-\frac{\mu}{\kappa}\mathbf{u}\right), \tag{A.5}$$

where $w_i = f_i^{eq}(\rho = 1, \mathbf{u} = \mathbf{0})$ and $c_s^2 = 1/3$ is an LBM lattice constant, and $\mu = \nu\rho_0$. As is usual in LBM methods, macroscopic quantities are expressed as moments of the distribution f_i. Here,

$$p = c_s^2 \sum_i f_i, \tag{A.6}$$

$$\mathbf{u} = \left(\rho_0 + \frac{1}{2}\frac{\mu}{\kappa}\right) \sum_i f_i \mathbf{e}_i. \tag{A.7}$$

Equation for concentration c is also solved using the LBM with a TRT scheme. The exact implementation follows Refs. [86, 104], and details of the method's performance for scalar transport problems can be found therein. For the 2D TRT model, the relaxation rates for the transport equation are given by

$$\Lambda_j^A = \begin{cases} \frac{\Lambda_A}{3D} & \text{for even moments,} \\ 3D & \text{for odd moments,} \end{cases} \tag{A.8}$$

where D is the diffusivity. To preserve the second-order trapezoidal scheme for pseudo-time advancement [104, 105] in the reaction term, the update rule for the transport equation is given by

$$g_i^{k+1}(\mathbf{x} + \mathbf{e}_i) = N_{ij}^{-1} \left\{ m_j^A - \left(\Lambda_j^A + \frac{1}{2}\right)^{-1} \left(m_j^A - m_j^{A,eq} - \Lambda_j^A Q_j\right) \right\},$$

where

$$Q_j = R m_j^{A,eq}(1, \mathbf{u}) \tag{A.9}$$

is the source term, g_i is the concentration PDF, and N_{ij} is the moment transformation matrix.

Acknowledgements The research was funded by the National Science Centre (NCN; Poland) under CEUS-UNISONO grant 2020/02/Y/ST3/00121. Computational resources were provided by Interdisciplinary Centre for Mathematical and Computational Modelling of University of Warsaw and by PL-Grid and LUMI consortium under Pilot-G project.
Authors would like to thank Maciej Szpindler, from LUMI support team, and Łukasz Łaniewski-Wołłk, author of TCLB, for making large-scale simulations possible.

References

1. Chadam, D., Hoff, D., Merino, E., Ortoleva, P., Sen, A.: Reactive infiltration instabilities. J. Appl. Math. **36**, 207–221 (1986)
2. Hoefner, M.L., Fogler, H.S.: Pore evolution and channel formation during flow and reaction in porous media. AIChE J. **34**, 45–54 (1988)
3. Jennings, J.N.: Karst geomorphology. Blackwell Oxford (1985)
4. De Waele, J., Lauritzen, S.E., Parise, M.: On the formation of dissolution pipes in quaternary coastal calcareous arenites in mediterranean settings. Earth Surf. Process. Landf. **36**, 143–157 (2011)
5. Lipar, M., Szymczak, P., White, S.Q., Webb, J.A.: Solution pipes and focused vertical water flow: Geomorphology and modelling, **218**, 103635. Earth-Sci, Rev (2021)
6. Chen, W., Ghaith, A., Park, A., Ortoleva, P.: Diagenesis through coupled processes: modeling approach, self-organization, and implications for exploration. APPG Mem. **49**, 103–130 (1990)
7. Boudreau, B.: Diagenetic Models and their Implementation. Springer (1996)
8. Aharonov, E., Whitehead, J., Kelemen, P., Spiegelman, M.: Channeling instability of upwelling melt in the mantle. J. Geophys. Res. **100**, 433–455 (1995)
9. Daines, M.J., Kohlstedt, D.L.: The transition from porous to channelized flow due to melt/rock reaction during melt migration. Geophys. Res. Lett. **21**, 145–148 (1994)
10. Merino, E., Banerjee, A.: Terra Rossa genesis, implications for Karst, and Eolian dust: A geodynamic thread. J. Geol. **116**, 62–75 (2008)

11. Hanna, R.B., Rajaram, H.: Influence of aperture variability on dissolutional growth of fissures in karst formations. Water Resour. Res. **34**, 2843–2853 (1998)
12. Groves, C.G., Howard, A.D.: Minimum hydrochemical conditions allowing limestone cave development. Water Resour. Res. **30**, 607–615 (1994)
13. Szymczak, P., Ladd, A.J.C.: The initial stages of cave formation: Beyond the one-dimensional paradigm. Earth Planet. Sci. Lett. **301**, 424–432 (2011)
14. Shalev, E., Lyakhovsky, V., Yechieli, Y.: Salt dissolution and sinkhole formation along the Dead Sea shore. J. Geophys. Res. **111**, B03102 (2006)
15. Ennis-King, J., Paterson, L.: Coupling of geochemical reactions and convective mixing in the long-term geological storage of carbon dioxide. Int. J. Greenhouse Gas Control **1**, 86–93 (2007)
16. Fryar, A.E., Schwartz, F.W.: Hydraulic-conductivity reduction, reaction-front propagation, and preferential flow within a model reactive barrier. J. Contam. Hydrol. **32**, 333–351 (1998)
17. Fredd, C.N., Fogler, H.S.: Influence of transport and reaction on wormhole formation in porous media. AIChE J. **44**, 1933–1949 (1998)
18. Economides, M.J., Nolte, K.G.: Reservoir Stimulation. John Wiley and Sons (2000)
19. Kalfayan, L.: Production Enhancement with Acid Stimulation. PenWell Corporation, Tulsa (2000)
20. Kalia, N., Balakotaiah, V.: Modeling and analysis of wormhole formation in reactive dissolution of carbonate rocks. Chem. Eng. Sci. **62**, 919–928 (2007)
21. Panga, M., Ziauddin, M., Balakotaiah, V.: Two-scale continuum model for simulation of wormhole formation in carbonate acidization. AIChE J. **51**, 3231–3248 (2005)
22. Cohen, C., Ding, D., Quintard, M., Bazin, B.: From pore scale to wellbore scale: Impact of geometry on wormhole growth in carbonate acidization. Chem. Eng. Sci. **63**, 3088–3099 (2008)
23. Szymczak, P., Ladd, A.J.C.: Wormhole formation in dissolving fractures. J. Geophys. Res. **114**, B06203 (2009)
24. Starchenko, V., Ladd, A.J.C.: The development of wormholes in laboratory scale fractures: perspectives from three-dimensional simulations. Water Resour. Res. **54**, 7946–7959 (2018)
25. Romanov, D., Gabrovšek, F., Dreybrodt, W.: Dam sites in soluble rocks: a model of increasing leakage by dissolutional widening of fractures beneath a dam. Eng. Geol. **70**, 129–145 (2003)
26. Fleury, V., Gouyet, J.F., Léonetti, M.: Branching in nature: dynamics and morphogenesis of branching structures, from cell to river networks. Springer Science & Business Media. (2013)
27. Polak, A., Elsworth, D., Liu, J., Grader, A.S.: Spontaneous switching of permeability changes in a limestone fracture with net dissolution. Water Resour. Res. **40**, W03502 (2004)
28. Noiriel, C., Gouze, P., Made, B.: 3D analysis of geometry and flow changes in a limestone fracture during dissolution. J. Hydrol. **486**, 211–223 (2013)
29. Luquot, L., Rodriguez, O., Gouze, P.: Experimental characterization of porosity structure and transport property changes in limestone undergoing different dissolution regimes. Transp. Porous Media **101**, 507–532 (2014)
30. Garcia-Rios, M., Luquot, L., Soler, J.M., Cama, J.: Influence of the flow rate on dissolution and precipitation features during percolation of CO2-rich sulfate solutions through fractured limestone samples. Chem. Geol. **414**, 95–108 (2015)
31. Luquot, L., Gouze, P.: Experimental determination of porosity and permeability changes induced by injection of CO2 into carbonate rocks. Chem. Geol. **265**, 148–159 (2009)
32. Ellis, B.R., Peters, C.A., Fitts, J.P., Bromhal, G.S., McIntyre, D., Warzinski, R., Rosenbaum, E.: Deterioration of a fractured carbonate caprock exposed to CO2-acidified brine flow. Greenhouse Gases Sci. Technol. **1**, 248–260 (2011)
33. Elkhoury, J.E., Ameli, P., Detwiler, R.L.: Dissolution and deformation in fractured carbonates caused by flow of CO2-rich brine under reservoir conditions. Int. J. Greenhouse Gas Control **16**, S203–S215 (2013)
34. Deng, H., Ellis, B.R., Peters, C.A., Fitts, J.P., Crandall, D., Bromhal, G.S.: Modifications of carbonate fracture hydrodynamic properties by CO2-acidified brine flow. Energy Fuels **27**, 4221–4231 (2013)
35. Smith, M., Sholokhova, Y., Hao, Y., Carroll, S.: CO2-induced dissolution of low permeability carbonates. Part I: Characterization and experiments. Adv. Water Res. **62**, 370–387 (2013)
36. Ott, H., Oedai, S.: Wormhole formation and compact dissolution in single-and two-phase CO2-brine injections. Geophys. Res. Lett. **42**, 2270–2276 (2015)
37. Menke, H., Andrew, M., Blunt, M., Bijeljic, B.: Reservoir condition imaging of reactive transport in heterogeneous carbonates using fast synchrotron tomography - Effect of initial pore structure and flow conditions. Chem. Geol. **428**, 15–26 (2016)
38. Szymczak, P., Ladd, A.J.C.: A network model of channel competition in fracture dissolution. Geophys. Res. Lett. **33**, L05401 (2006)
39. Budek, A., Szymczak, P.: Network models of dissolution of porous media. Phys. Rev. E **86**, 056318 (2012)
40. Walsh, P., Morawiecka-Zacharz, I.: A dissolution pipe palaeokarst of Mid-Pleistocene age preserved in Miocene limestones near Staszów, Poland. Palaeogeogr. Palaeoclimatol. Palaeoecol. **174**, 327–350 (2001)
41. Rohmer, J., Aochi, H.: Impact of channel-like erosion patterns on the frequency-magnitude distribution of earthquakes. Geophys. J. Int. **202**, 670–677 (2015)
42. Békri, S., Thovert, J.F., Adler, P.M.: Dissolution of porous media. Chem. Eng. Sci. **50**, 2765–2791 (1995)

43. Szymczak, P., Ladd, A.J.C.: Microscopic simulations of fracture dissolution. Geophys. Res. Lett. **31**, L23606 (2004)
44. Yu, D., Ladd, A.J.C.: A numerical simulation method for dissolution in porous and fractured media. J. Comput. Phys. **229**, 6450–6465 (2010)
45. Yoon, H., Valocchi, A.J., Werth, C.J., Dewers, T.: Pore-scale simulation of mixing-induced calcium carbonate precipitation and dissolution in a microfluidic pore network. Water Resour. Res. **48**, W02524 (2012)
46. Chen, L., Kang, Q., Viswanathan, H.S., Tao, W.Q.: Pore-scale study of dissolution-induced changes in hydrologic properties of rocks with binary minerals. Water Resour. Res. **50**, 9343–9365 (2014)
47. Pereira Nunes, J.P., Blunt, M.J., Bijeljic, B.: Pore-scale simulation of carbonate dissolution in micro-CT images. J. Geophys. Res. Solid Earth **121**, 558–576 (2016)
48. Soulaine, C., Roman, S., Kovscek, A., Tchelepi, H.A.: Mineral dissolution and wormholing from a pore-scale perspective. J. Fluid Mech. **827**, 457–483 (2017)
49. Deng, H., Steefel, C., Molins, S., DePaolo, D.: Fracture evolution in multimineral systems: The role of mineral composition, flow rate, and fracture aperture heterogeneity. ACS Earth Space Chem. **2**, 112–124 (2018)
50. Molins, S., Soulaine, C., Prasianakis, N.I., Abbasi, A., Poncet, P., Ladd, A.J.C., Starchenko, V., Roman, S., Trebotich, D., Tchelepi, H.A., Steefel, C.I.: Simulation of mineral dissolution at the pore scale with evolving fluid-solid interfaces: review of approaches and benchmark problem set. Comput. Geosci. **25**, 1285–1318 (2021)
51. Steefel, C.I., Appelo, C.A.J., Arora, B., Jacques, D., Kalbacher, T., Kolditz, O., Lagneau, V., Lichtner, P.C., Mayer, K.U., Meeussen, J.C.L., Molins, S., Moulton, D., Shao, H., Šimůnek, J., Spycher, N., Yabusaki, S.B., Yeh, G.T.: Reactive transport codes for subsurface environmental simulation. Comput. Geosci. **19**, 445–478 (2015)
52. Mayer, K.U., Alt-Epping, P., Jacques, D., Arora, B., Steefel, C.I.: Benchmark problems for reactive transport modeling of the generation and attenuation of acid rock drainage. Comput. Geosci. **19**, 599–611 (2015)
53. Lichtner, P.C., Hammond, G.E., Lu, C., Karra, S., Bisht, G., Andre, B., Mills, R., Kumar, J.: PFLOTRAN user manual: A massively parallel reactive flow and transport model for describing surface and subsurface processes. Report. Los Alamos National Lab. (LANL), Los Alamos, NM (United States); Sandia (2015)
54. Xu, T., Sonnenthal, E., Spycher, N., Pruess, K.: TOUGHREACT - a simulation program for non-isothermal multiphase reactive geochemical transport in variably saturated geologic media: applications to geothermal injectivity and CO2 geological sequestration. Comput. Geosci. **32**, 145–165 (2006)
55. Battiato, I., Tartakovsky, D.M.: Applicability regimes for macroscopic models of reactive transport in porous media. J. Contam. Hydrol. **120–121**, 18–26 (2011)
56. Boso, F., Battiato, I.: Homogenizability conditions for multicomponent reactive transport. Adv. Water Res. **62**, 254–265 (2013)
57. Ladd, A.J., Szymczak, P.: Reactive Flows in Porous Media: Challenges in Theoretical and Numerical Methods. Annu. Rev. Chem. Biomol. Eng. **12**, 543–571 (2021)
58. De Boever, E., Varloteaux, C., Nader, F.H., Foubert, A., Békri, S., Youssef, S., Rosenberg, E.: Quantification and prediction of the 3D pore network evolution in carbonate reservoir rocks. Oil Gas Sci. Technol. **67**, 161–178 (2012)
59. Varloteaux, C., Vu, M.T., Békri, S., Adler, P.M.: Reactive transport in porous media: pore-network model approach compared to pore-scale model. Phys. Rev. E **87**, 023010 (2013)
60. Cheung, W., Rajaram, H.: Dissolution finger growth in variable aperture fractures: Role of the tip-region flow field. Geophys. Res. Lett. **29**, 2075 (2002)
61. Kalia, N., Balakotaiah, V.: Effect of medium heterogeneities on reactive dissolution of carbonates. Chem. Eng. Sci. **64**, 376–390 (2009)
62. Maheshwari, P., Balakotaiah, V.: Comparison of carbonate HCl acidizing experiments with 3D simulations. SPE Prod. Oper. **28**, 402–413 (2013)
63. Upadhyay, V.K., Szymczak, P., Ladd, A.J.C.: Initial conditions or emergence: What determines dissolution patterns in rough fractures? J. Geophys. Res. Solid Earth **120**, 6102–6121 (2015)
64. Pereira Nunes, J., Bijeljic, B., Blunt, M.: Pore-space structure and average dissolution rates: A simulation study. Water Resour. Res. **52**, 7198–7212 (2016)
65. Cooper, M.P., Sharma, R.P., Magni, S., Blach, T.P., Radlinski, A.P., Drabik, K., Tengattini, A., Szymczak, P.: 4D tomography reveals a complex relationship between wormhole advancement and permeability variation in dissolving rocks. Adv. Water Res. **175**, 104407 (2023)
66. Izgec, O., Zhu, D., Hill, A.D.: Numerical and experimental investigation of acid wormholing during acidization of vuggy carbonate rocks. J. Pet. Sci. Eng. **74**, 51–66 (2010)
67. Brinkman, H.C.: A calculation of the viscous force exerted by a flowing fluid on a dense swarm of particles. Appl. Sci. Res. A **1**, 27–34 (1947)
68. Lundgren, T.S.: Slow flow through stationary random beds and suspensions of spheres. J. Fluid Mech. **51**, 273–299 (1972)
69. Durlofsky, L., Brady, J.: Analysis of the Brinkman equation as a model for flow in porous media. Phys. Fluids **30**, 3329–3341 (1987)
70. Golfier, F., Zarcone, C., Bazin, B., Lenormand, R., Lasseux, D., Quintard, M.: On the ability of a Darcy-scale model to capture wormhole formation during the dissolution of a porous medium. J. Fluid Mech. **457**, 213–254 (2002)

71. Szymczak, P., Ladd, A.J.C.: Interacting length scales in the reactive-infiltration instability. Geophys. Res. Lett. **40**, 3036–3041 (2013)
72. Shi, B., Guo, Z.: Lattice Boltzmann model for nonlinear convection-diffusion equations. Phys. Rev. E **79**, 016701 (2009)
73. Guo, X., Shi, B., Chai, Z.: General propagation lattice Boltzmann model for nonlinear advection-diffusion equations. Phys. Rev. E **97**, 043310 (2018)
74. Dreybrodt, W.: The role of dissolution kinetics in the development of karst aquifers in limestone: A model simulation of karst evolution. J. Geol. **98**, 639–655 (1990)
75. Colombani, J.: Measurement of the pure dissolution rate constant of a mineral in water. Geochim. Cosmochim. Acta **72**, 5634–5640 (2008)
76. Bear, J.: Dynamics of fluids in porous media. Dover (1972)
77. Noiriel, C., Luquot, L., Madé, B., Raimbault, L., Gouze, P., van der Lee, J.: Changes in reactive surface area during limestone dissolution: An experimental and modelling study. Chem. Geol. **265**, 160–170 (2009)
78. Ladd, A.J.C., Szymczak, P.: Use and misuse of large-density asymptotics in the reaction-infiltration instability. Water Resour. Res. **53**, 2419–2430 (2017)
79. Szymczak, P., Ladd, A.J.C.: Instabilities in the dissolution of a porous matrix. Geophys. Res. Lett. **38**, L07403 (2011)
80. Golfier, F., Quintard, M., Whitaker, S.: Heat and mass transfer in tubes: An analysis using the method of volume averaging. J. Porous Media **5**, 169–185 (2002)
81. Ortoleva, P., Merino, E., Moore, C., Chadam, J.: Geochemical self-organization I: Reaction-transport feedbacks and modeling approach. Am. J. Sci. **287**, 979–1007 (1987)
82. Łaniewski-Wołłk, Ł, Rokicki, J.: Adjoint lattice Boltzmann for topology optimization on multi-GPU architecture. Comput. Math. Appl. **71**, 833–848 (2016)
83. Guo, Z., Zhao, T.S., Shi, Y.: Preconditioned lattice-Boltzmann method for steady flows. Phys. Rev. E **70**, 066706 (2004)
84. Ginzburg, I.: Consistent lattice Boltzmann schemes for the Brinkman model of porous flow and infinite Chapman-Enskog expansion. Phys. Rev. E **77**, 066704 (2008)
85. Ginzburg, I.: Equilibrium-type and link-type lattice Boltzmann models for generic advection and anisotropic-dispersion equation. Adv. Water Res. **28**, 1171–1195 (2005)
86. Gruszczyński, G.: Łaniewski-Wołłk, Ł: A comparative study of 3D cumulant and central moments lattice Boltzmann schemes with interpolated boundary conditions for the simulation of thermal flows in high Prandtl number regime. Int. J. Heat Mass Transf. **197**, 123259 (2022)
87. Ginzburg, I., Silva, G., Talon, L.: Analysis and improvement of Brinkman lattice Boltzmann schemes: Bulk, boundary, interface. similarity and distinctness with finite elements in heterogeneous porous media. Phys. Rev. E **91**, 023307 (2015)
88. Kang, D.H., Yang, E., Yun, T.S.: Stokes-Brinkman flow simulation based on 3-D μ-CT images of porous rock using grayscale pore voxel permeability. Water Resour. Res. **55**, 4448–4464 (2019)
89. van Duijn, C.J., Knabner, P.: Travelling wave behaviour of crystal dissolution in porous media flow. Eur. J. Appl. Math. **8**, 49–72 (1997)
90. Chadam, J., Chen, X., Comparini, E., Ricci, R.: Travelling wave solutions of a reaction-infiltration problem and a related free boundary problem. Eur. J. Appl. Math. **5**, 255–265 (1994)
91. Kondratiuk, P., Tredak, H., Ladd, A.J.C., Szymczak, P.: Synchronization of dissolution and precipitation fronts during infiltration-driven replacement in porous rocks. Geophys. Res. Lett. **42**, 2244–2252 (2015)
92. Hindmarsh, A.: ODEPACK, A Systematized Collection of ODE Solvers, in R.S. Stepleman et al. (eds.), North-Holland, Amsterdam, (vol. 1 of IMACS Transactions on Scientific Computation), pp. 55–64. (1983)
93. Bogacki, P., Shampine, L.F.: A 3(2) pair of Runge - Kutta formulas. Appl. Math. Lett. **2**, 321–325 (1989)
94. Szymczak, P., Ladd, A.J.C.: Stochastic boundary conditions to the convection-diffusion equation including chemical reactions at solid surfaces. Phys. Rev. E **69**, 036704 (2004)
95. Zaninetti, L.: A left and right truncated lognormal distribution for the stars. Adv. Astrophys. **2**, 197–213 (2017)
96. Saupe, D.: Algorithms for random fractals. In: Peitgen, H.O., Saupe, D. (eds.) The Science of Fractal Images, pp. 71–136. Springer, New York, New York, NY (1988)
97. Mahrous, M., Curti, E., Churakov, S.V., Prasianakis, N.I.: Petrophysical initialization of core-scale reactive transport simulations on Indiana limestones: Pore-scale characterization, spatial autocorrelations, and representative elementary volume analysis. J. Pet. Sci. Eng. **213**, 110389 (2022)
98. Koval, E.: A method for predicting the performance of unstable miscible displacement in heterogeneous media. Soc. Petrol. Eng. J. **3**, 145–154 (1963)
99. Booth, R.: On the growth of the mixing zone in miscible viscous fingering. J. Fluid Mech. **655**, 527–539 (2010)
100. An, S., Hasan, S., Erfani, H., Babaei, M., Niasar, V.: Unravelling effects of the pore-size correlation length on the two-phase flow and solute transport properties: GPU-based pore-network modeling. Water Resour. Res. **56**, e2020WR027403 (2020)
101. Al-Khulaifi, Y., Lin, Q.Y., Blunt, M.J., Bijeljic, B.: Reaction rates in chemically heterogeneous rock: Coupled impact of structure and flow properties studied by X-ray microtomography. Environ. Sci. Technol. **51**, 4108–4116 (2017)

102. Menke, H.P., Reynolds, C.A., Andrew, M.G., Nunes, J.P.P., Bijeljic, B., Blunt, M.J.: 4D multi-scale imaging of reactive flow in carbonates: Assessing the impact of heterogeneity on dissolution regimes using streamlines at multiple length scales. Chem. Geol. **481**, 27–37 (2018)
103. Wang, Y.D., Chung, T., Armstrong, R.T., Mostaghimi, P.: ML-LBM: Predicting and Accelerating Steady State Flow Simulation in Porous Media with Convolutional Neural Networks. Transp. Porous Media **138**, 49–75 (2021)
104. Gruszczyński, G., Dzikowski, M., Łaniewski -Wołłk, Ł.: Revisiting the second-order convergence of the lattice Boltzmann method with reaction-type source terms. Comput. Math. Appl. **144**, 34–50 (2023)
105. He, X., Chen, S., Doolen, G.D.: A novel thermal model for the Lattice Boltzmann Method in incompressible limit. J. Comput. Phys. **146**, 282–300 (1998)

Authors and Affiliations

Michał Dzikowski[1,2] · **Piotr Szymczak**[1]

✉ Michał Dzikowski
mj.dzikowsk2@uw.edu.pl

Piotr Szymczak
piotrek@fuw.edu.pl

[1] Institute of Theoretical Physics, Faculty of Physics, University of Warsaw, Warsaw, Poland

[2] Interdisciplinary Centre for Mathematical and Computational Modelling, University of Warsaw, Warsaw, Poland